# Properties of the Pt(111)/Electrolyte Electrochemical Interface Studied with a Hybrid DFT–Solvation Approach

Rebekka Tesch,[1,2,3] Piotr M. Kowalski,[1,3] and Michael H. Eikerling[1,2,3]

[1]*Institute of Energy and Climate Research, Theory and Computation of Energy Materials (IEK-13), Forschungszentrum Jülich GmbH, 52425 Jülich, Germany*

[2]*Chair of Theory and Computation of Energy Materials, Faculty of Georesources and Materials Engineering, RWTH Aachen University, 52062 Aachen, Germany*

[3]*Jülich Aachen Research Alliance, JARA-CSD and JARA-ENERGY, 52425 Jülich, Germany*

(Dated: July 21, 2021)

## Abstract

Self-consistent modeling of the interface between a solid metal electrode and a liquid electrolyte is a crucial challenge in computational electrochemistry. In this contribution, we adopt the ESM-RISM computational framework to study the charged interface between a Pt(111) surface partially covered with chemisorbed oxygen and an aqueous acidic electrolyte. This method proves to be well suited to control the electrode potential and describe the chemisorption and charging state of the interface. We present an in-depth assessment of the ESM-RISM parameterization and of the importance of computing near-surface water molecules explicitly at the quantum mechanical level. We found that ESM-RISM is able to reproduce some key interface properties, including the peculiar, non-monotonic charging relation of the Pt(111)/electrolyte interface. The comparison with independent theoretical models and explicit simulations of the interface shows strengths and limitations of ESM-RISM for modeling of electrochemical interfaces.


## I. INTRODUCTION

The transition to a defossilized energy economy depends on the development of highly performing and economically viable water electrolysers and hydrogen fuel cells for the production and use of green hydrogen [1–5]. Building advanced electrochemical devices requires ground-breaking progress at the materials science frontier, to generate fundamental understanding of the relations between structure, properties and performance of materials and to enable the design of functionally optimized materials. Atomic-scale understanding of the structure and dynamics at the interface between a solid electrode and a liquid electrolyte under an applied electrode potential is a crucial aspect in this context [6–12]. However, experimental studies are difficult to perform at this scale. Atomistic simulations therefore play an important role in understanding the properties of this interface [6, 13, 14].

Despite major efforts over the last two decades, a simulation approach to self-consistently model the electrode/electrolyte interface with the required accuracy and at a reasonable computational cost does not yet exist [15, 16]. The major challenges are: (1) to compute an electrode under an applied electrode potential, meaning that the number of electrons in the system is allowed to vary, and to pin this potential to an experimental potential scale; (2) to take into account electrostatic as well as electronic solvent and electrolyte effects and perform a proper thermodynamic sampling of solvent configurations; (3) to describe the

non-linear coupling of interdependent phenomena at the solid electrode/liquid electrolyte boundary.

Computational approaches nowadays routinely describe the solid metal electrode at the level of density functional theory (DFT), but differ in the way the electrolyte and electric field effects are taken into account. An extensive review of currently available methods has recently been provided by Schwarz and Sundararaman [15]. The widely used computational hydrogen electrode (CHE) [17] introduces the effect of the electrode potential *a posteriori* by adding a correction term, $eU$, to the reaction Gibbs energy of any elementary surface reaction step that involves an electron transfer, where $U$ is the electrode potential. Different treatments for charged surface configurations and potential effects have been proposed [18–22]. The original variant of the CHE and other DFT-based approaches [18, 21, 23–25] consider the state of the electrode at constant charge (i.e. at a fixed number of electrons), while experiments are conducted at constant electrode potential. A constant electrode potential is realized in grand canonical computational schemes that allow the number of electrons and electrolyte ions to vary [22, 26–28].

First-principles methods in electrochemistry differ in the treatment of solvent and electrolyte[1] effects [15]. Computing the entire system explicitly at the DFT level, as done in *ab initio* molecular dynamics (AIMD) simulations, would in principle provide an accurate treatment of the electrolyte [29, 30]. However, AIMD simulations are computationally demanding and practicable only for short time and length scales. These scales are usually insufficient for meaningful computational studies of electrochemical interfaces, including electrolytes with low concentrations of ions [15]. Therefore, most approaches employ hybrid schemes to compute electrode and electrolyte at different levels of theory. They treat the solid electrode at the DFT level and the electrolyte with force field-based molecular dynamics (MD), corresponding to so-called QM/MM approaches [31, 32]. Another type of approach employs implicit or continuum solvation models (CSM) for the electrolyte region [33–37]. In these computationally efficient approaches, solvent molecules and electrolyte ions are replaced by a uniform polarizable medium with continuous ion density distribution. This implies that any structural information on the molecular entities of the electrolyte and their local arrangement is lost. In the implicit models, electrolyte ion density distributions

[1] Note that in the following, by "electrolyte" we denote the electrolyte solution consisting of solvent and electrolyte ions.

as a function of potential distribution are most commonly described by either standard or modified Poisson-Boltzmann approaches [38]. Many of these models [34–37] place the solute, namely the electrode slab, into a cavity, which remains electrolyte-free. Cavity-based implicit solvent models have been developed originally for the solvation of small, neutral solute molecules [39, 40]. They might therefore not be suitable to describe solvation phenomena at metal surfaces.

Non-cavity based implicit solvation models rely on the integral equation theory of liquids or classical density functional theory. The former is the case for the Reference Interaction Site Method (RISM) [41, 42], whereas the latter approach is implemented in joint density functional theory (JDFT) [43]. In contrast to standard cavity-based implicit solvation approaches, these approaches capture features of the statistical liquid distribution [44, 45]. Further partitioning of the electrolyte region could combine explicit and implicit treatments of solvation effects. Hybrid models aim at providing a more accurate description of an interface by including a few explicit electrolyte species at the DFT level, while treating the rest of the electrolyte by implicit models [46].

The study presented here adopts the effective screening medium reference interaction site method of Otani and coworkers (ESM-RISM) [44]. This method combines a quantum mechanical description of the solid electrode, at the level of DFT, with the classical theory of liquids in the RISM framework for the electrolyte region. The periodic boundary condition in the spatial direction perpendicular to the plane of the electrode slab is lifted by replacing the periodic images of the simulation cell by vacuum using the ESM approach [20]. It thereby avoids spurious electrostatic interactions between the periodically repeated images of the simulated interface model.

ESM-RISM gives distribution functions of solvent molecules and electrolyte ions and the local electrical potential at the interface [44, 45], thus providing important information on the structure and properties of the electrochemical double layer. We employ an implementation that includes a potentiostat [26] to simulate the effect of electrode potential within a grand canonical ensemble. The potential in the bulk electrolyte serves as the reference electrode potential [44]. Any slab charge is screened by the electrolyte, so that charge neutrality is always guaranteed without having to add any countercharge. The method is computationally efficient due to the classical force field-based treatment of electrolyte–electrolyte and electrode–electrolyte interactions and due to the mixed boundary conditions that allow to

use relatively small simulation cells [20, 44]. However, RISM is an implicit electrolyte model that does not provide any information on the electronic configuration of the electrolyte and its ionic configuration is described only in an average, statistical way. Electroactive molecules that undergo reactive processes at the metal surface must be considered explicitly at the quantum mechanical level, i.e. as part of the DFT region. With a proper partitioning into explicit quantum mechanical region and classical continuum region, ESM-RISM is well suited to describe, at least qualitatively, electrolyte phenomena at the electrode/electrolyte interface and it has been successfully used to simulate electrochemical systems [45, 47–49].

We computed properties of the widely studied Pt(111)/electrolyte interface [13, 50, 51]. Depending on applied potential and electrolyte composition, the Pt(111) surface is known to be covered by varying types and amounts of adsorbates [52]. This allows to pin the potential to the surface structure, by adding a variant number of adsorbed atoms to the surface [53–55]. We first studied the RISM description of pure bulk water. This is followed by thorough tests of various input parameters for the ESM-RISM interface calculation setup, including the geometric arrangement of the solid electrode and liquid electrolyte in the simulation cell and the interaction parameters that describe electrode–electrolyte interactions. In the last step, we computed various interface properties, such as electrostatic potential profiles and metal charging relations.

## II. METHODS

We computed clean as well as partially oxidized Pt(111) surfaces in pure water and aqueous HCl electrolyte. All calculations were performed with the plane-wave Quantum ESPRESSO software package, version 6.4 [56], modified by Nishihara and Otani [44] to implement the ESM-RISM interface model. We used the PBE exchange-correlation functional [57] to directly compare our results with previous studies of Fernandez-Alvarez and Eikerling [55]. For systems with explicit water we used the revPBE exchange-correlation functional [58] in conjunction with the D3 dispersion correction [59]. This functional is known to give very similar results to the RPBE-D3 functional [60, 61], which reliably describes water structures at the Pt(111)/water interface [62]. However, the latter functional is not implemented in the standard version of Quantum ESPRESSO. Core electrons were described by ultrasoft pseudopotentials, with the Pt $6s^1 5d^9$, O $2s^2 2p^4$ and H $1s^1$ electrons computed

explicitly. All calculations were spin-unpolarized, with energy cutoffs of 40 Ry and 320 Ry for plane waves and charge density, respectively. Gaussian broadening by 0.015 Ry was used for orbital occupations. Geometries were optimized with convergence thresholds of $10^{-4}$ Ry and $10^{-3}$ Ry/$a_0$ (where $a_0$ is the Bohr radius) for energy and forces, respectively.

RISM computes electrolyte–electrolyte and electrode–electrolyte correlation functions by solving the Ornstein–Zernike equation and a suitable closure relation self-consistently [42]. The closure equation contains an interparticle interaction potential $u_{\alpha\gamma}$ that describes the interactions between particles of type $\alpha$ and $\gamma$ in the electrolyte–electrolyte and electrode–electrolyte systems. In the ESM-RISM scheme applied here, the interaction potential $u_{\alpha\gamma}$ is of Lennard-Jones (LJ) type and contains a separate term for Coulomb interactions, given by

$$u_{\alpha\gamma} = 4\varepsilon_{\alpha\gamma}\left[\left(\frac{\sigma_{\alpha\gamma}}{r}\right)^{12} - \left(\frac{\sigma_{\alpha\gamma}}{r}\right)^{6}\right] + \frac{q_\alpha q_\gamma}{r} \ . \tag{1}$$

For the interactions between particles of different type, we apply the classical Lorentz–Berthelot mixing rules: $\sigma_{\alpha\gamma} = \frac{\sigma_\alpha + \sigma_\gamma}{2}$ and $\varepsilon_{\alpha\gamma} = \sqrt{\varepsilon_\alpha \varepsilon_\gamma}$ [63]. The choice of LJ parameters directly determines the system's correlation functions via the closure relation. In the first step of a RISM calculation, electrolyte–electrolyte correlation functions are computed in the 1D-RISM framework [44]. When computing molecules in electrolyte solution, the 3D-RISM [64] is then used to obtain the solute–electrolyte correlations. For computation of interfaces we applied the Laue-RISM scheme in the ESM framework, called ESM-RISM [44].

The computation of a single water molecule in aqueous solvent was performed using a cubic box of 20 Å length and the 3D-RISM framework with the Kovalenko–Hirata (KH) closure relation [65]. A single $k$-point (the $\Gamma$ point) was used in this case. The solvent temperature was set to 300 K and the cutoff energy for solvent correlation functions was 160 Ry. Solvent water of density 1 g/cm$^3$ was described by the TIP5P [66] and SPC [67] water models. It should be noted that the original water models are modified in the RISM framework by adding LJ parameters of $\varepsilon = 0.046$ kcal/mol and $\sigma = 1.0$ and 1.8 Å at the H and oxygen lone pair (L) sites, respectively [45, 68–70]. The LJ parameters for the solute water molecule were $\varepsilon_{\mathrm{O}} = 0.1554$ kcal/mol, $\sigma_{\mathrm{O}} = 3.166$ Å [71], $\varepsilon_{\mathrm{H}} = 0.0460$ kcal/mol and $\sigma_{\mathrm{H}} = 1.0$ Å. Convergence thresholds for the 1D-RISM and 3D-RISM were $10^{-8}$ Ry and $10^{-6}$ Ry, respectively.

Interface calculations were performed in a vacuum/slab/electrolyte configuration (see Figure 1). In the direction perpendicular to the metal slab, the DFT unit cell is bounded

by effective screening media (vacuum in this case) at both ends. The metal slab adjoins vacuum at its left side; at its right side, the electrolyte region extends, starting from the position set by the `laue_starting_right` parameter. The electrode/electrolyte interface is located at the metal slab's right side in this asymmetric setup. Beyond the DFT cell, the electrolyte region extends further, as determined by the `laue_expand_right` parameter.

Converged interfacial properties were obtained with a DFT cell length of 60 Å. The left vacuum region was 10 Å thick. The right solvent region was extended beyond the DFT cell by ∼32 Å, i.e. up to ∼75 Å from the Pt surface slab. Vacuum layers as well as dipole correction schemes are not needed in the ESM scheme, because the simulation cell is not periodically repeated in the direction perpendicular to the slab. If not explicitly mentioned in the text, the parameter limiting the extend of the solvent region slab-sided (`laue_starting_right`) was set between the two outermost atomic layers of the Pt slab, as suggested by Haruyama *et al.* [45]. Optimized Pt bulk lattice constants of 3.981 and 3.996 Å were used in calculations with the PBE and revPBE-D3 functionals, respectively.

The Pt(111) surface was modeled by slabs of four layers thickness. The two bottom layers were fixed to bulk positions. The computed surface unit cell was a $2\sqrt{3} \times 2\sqrt{3}$ cell with 12 surface Pt atoms. A Monkhorst–Pack [72] $k$-point mesh of 4×4×1 was applied. Different oxygen coverages from 0 to 3/4 ML were modeled by adding varying numbers of adsorbed oxygen atoms in the fcc hollow sites of Pt(111). The oxygen atoms were evenly distributed on the surface sites. The electrolyte region was filled by either pure water (described by the TIP5P model) or by aqueous HCl with a concentration of 0.1 or 1 mol/L. The closure relation, solvent temperature, solvent correlation functions cutoff and RISM convergence thresholds were the same as in the case of the solvated water molecule. Different LJ parameters were used for solute Pt and O atoms (see Table II), as will be described in Section III B. LJ parameters for the electrolyte ions $Cl^-$ and $H_3O^+$ were $\varepsilon_{Cl} = 0.1001$ kcal/mol, $\sigma_{Cl} = 4.4$ Å [73], $\varepsilon_O = 0.1554$ kcal/mol, $\sigma_O = 3.166$ Å [74], $\varepsilon_H = 0.0460$ kcal/mol and $\sigma_H = 0.4$ Å [74].

In calculations with one water layer computed explicitly by DFT, we used an ice-like hexagonal bilayer water structure with H-up and H-down structural arrangements. In both cases, 8 water molecules were added per surface unit cell, resulting in a water coverage of 2/3 (see Figure 4). LJ parameters for the explicit O and H atoms of these water molecules were the same as in the pure water simulations.

Simulations with applied potential were performed in a grand canonical ensemble [26].

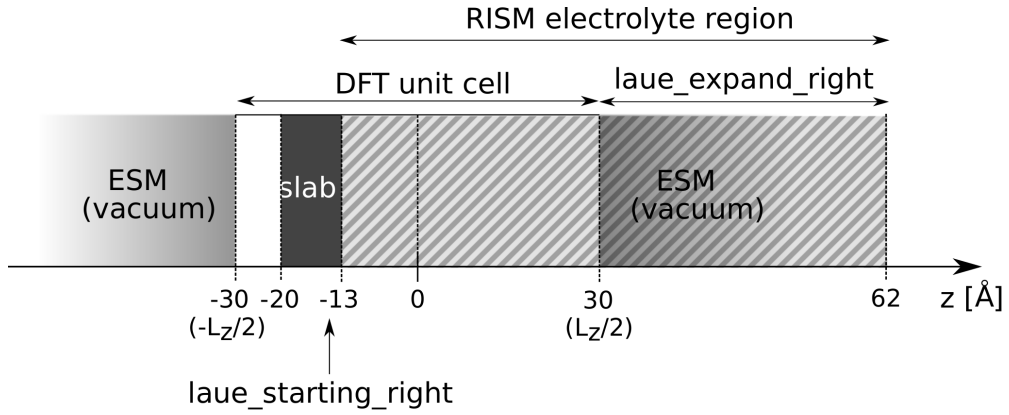


FIG. 1. Schematic representation of the computational setup for ESM-RISM calculations of an electrochemical interface. The simulated system consists of a vacuum region, a metal slab and an electrolyte region. The schematic also indicates the regions for the effective screening medium (ESM) at both sides of the DFT unit cell as well as the metal slab position in the DFT unit cell. The scale shows the dimensions of the respective regions as used in this work.

The system was coupled to an electron reservoir in a potentiostat scheme. The grand potential, $\Omega$, was minimized, which contains the potentiostat contribution $\mu\Delta N$, where $\mu$ is the chemical potential of electrons (Fermi energy) and $\Delta N$ is the excess number of electrons at a particular potential $\mu$ compared to a neutral metal slab,

$$\Omega = E - \mu\Delta N. \tag{2}$$

We computed the surface at a given potential by fixing the Fermi energy. A shift in the Fermi energy, $\Delta\mu$, is related to a shift in the electrode potential, $\Delta\varphi$, by $\Delta\mu = -e\Delta\varphi$. The code reaches the target Fermi energy by adapting the slab charge in a fictitious charge particle (FCP) dynamics scheme. The convergence threshold for the forces in the FCP relaxation was set to 0.01 eV. In ESM-RISM, the resulting total slab charge is fully compensated by the electrolyte charge of equal size and opposite sign, so that the system is electroneutral overall. The electrostatic potential in bulk electrolyte serves as a potential reference.

## III. RESULTS AND DISCUSSION

### A. Water model

The accurate description of electrolyte–electrolyte interactions is a prerequisite for the correct description of electrode/electrolyte interfaces. Therefore, we first computed properties of pure water solvent. This basic inspection does not involve an interface, but serves to test the water model used in RISM for consistency. Describing the structure of water is a challenge in itself for molecular simulations [75–77]. To test the performance of RISM, in the first step we computed a single, solvated (hydrated) water molecule. We calculated water–water pair distribution functions (with 1D-RISM) and hydration free energies of the water molecule (with 3D-RISM). The resulting pair distribution functions are shown in Figure 2. They show the typical qualitative features of the hydrogen bonded network in water [78], yet deviate visibly from experimental results in terms of peak positions and peak shapes. Our results are consistent with other RISM studies of water [64, 79]. We note the significant offset between computed and measured maxima of O–O pair distribution functions. This occurs because water in the first hydration shell exhibits structural ordering which cannot be preserved with the statistical averaging involved in a RISM calculation. Comparison to classical molecular dynamics (cMD) simulations with the same water models (see Figure S1) shows that the deficiency in describing the water structure is indeed related to RISM, and not to the water model itself. To adequately represent the structural organization and electrostatic properties of water, water molecules of the first hydration shell have to be treated explicitly at the level of quantum mechanical calculations.

Hydration free energies play an important role in electrochemical systems and should be reproduced with sufficient accuracy by a chosen water model [45]. As shown in Table I, hydration free energies computed with RISM using the TIP5P water model agree better with experiment than those computed with the simpler SPC model. Therefore, we used the TIP5P model in the subsequently reported studies.

### B. ESM-RISM electrode–electrolyte model

Several parameters have to be set in the ESM-RISM approach so that it will provide consistent and insightful results for the Pt(111)/electrolyte interface. These include the

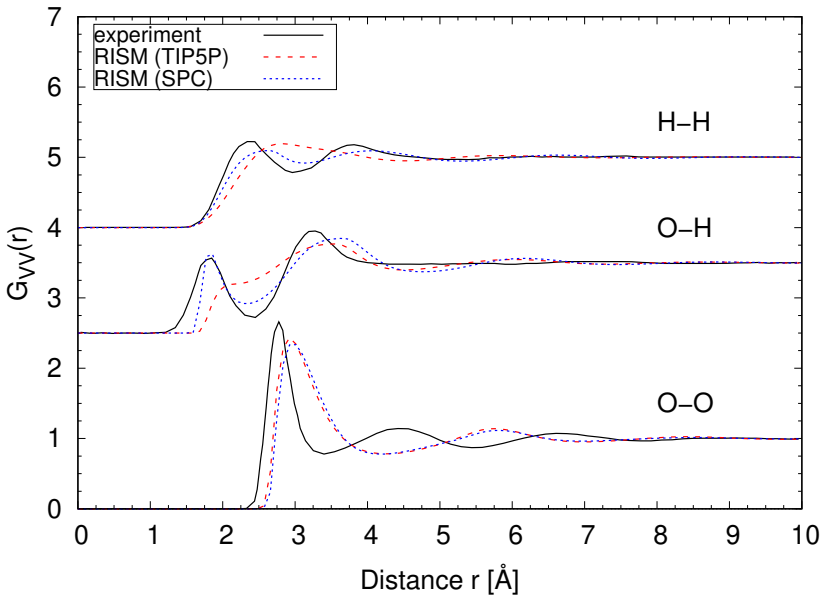


FIG. 2. Water–water pair distribution functions computed with 1D-RISM applying TIP5P and SPC water models. Neutron scattering experimental data [78] are shown for comparison.

TABLE I. Hydration free energies of a water molecule in implicit water solvent computed with 3D-RISM with different water models.

| Method | Hydration free energy [kcal/mol] |
|---|---|
| 3D-RISM SPC | -4.1 |
| 3D-RISM TIP5P | -5.2 |
| 3D-RISM SPC [44] | -4.2 |
| experiment [80] | -6.3 |

simulation cell size, the width and starting position of the solvent region (see Figure 1) and the LJ parameters for interactions between electrode and electrolyte.

Too small simulation cell and/or solvent region sizes can affect interfacial properties such as electrostatic potential profiles (see Figures S1 and S2 in the Supplementary Information). This is because in small model systems direct correlation functions are truncated at too short distances [44]. We therefore used large DFT unit cells of 60 Å length with the solvent region expanding ∼32 Å further, beyond the DFT cell.

Another important ESM-RISM input parameter, which is discussed in the literature [45, 55], is the starting position of the solvent region at the right side of the slab in the

vacuum/slab/electrolyte setup (`laue_starting_right`, see Figure 1). An infinitely high wall potential prevents the solvent from extending to the left of this point. The actual electrode–electrolyte separation distance (or gap width) is determined by the LJ interaction between electrode atoms and electrolyte species. The statistical distribution of solvent and electrolyte is an outcome of the self-consistent solution of the Ornstein–Zernike equation, as implemented in RISM. The `laue_starting_right` parameter should be located close to the interface, on the electrode side, preferably between the first and second layers of atoms in the metal slab [45]. In contrast, when the `laue_starting_right` parameter is set too far from the Pt surface, an artificial vacuum between slab and solvent is created (see Figure S4), which has a significant impact on interfacial solvent distribution functions (see Figure S4), interfacial potential (see Figure S5) and other computed interface properties. The relative position of electrode and electrolyte is of utmost importance for electrochemical interfaces [15, 81, 82] and therefore should be carefully computed.

An energy minimization procedure has been used in the literature to determine the `laue_starting_right` parameter [55]. The ESM-RISM solvation energy as a function of `laue_starting_right` shows a clearly discernible minimum (see Figure S5). The increase in solvation energy with increasing `laue_starting_right` is induced by too large (and thus unfavorable) electrode–electrolyte separation. On the other hand, the solvation energy increase with decreasing `laue_starting_right` is probably related to a very small (and unphysical) amount of solvent that extends into the metal slab, despite the infinitely high repulsive wall, experiencing highly repulsive interactions. This puts energy minimization procedures to find the correct `laue_starting_right` [55] into question. As can be seen from Figures S3, S4 and S5, the value of `laue_starting_right` that would result from an energy minimization procedure is too large and introduces the aforementioned artificial vacuum layer between slab and solvent. We stress that in this work, the `laue_starting_right` parameter is not obtained from an energy minimization procedure, but set between the two outermost atomic layers of the Pt slab. The electrode–electrolyte gap is then computed self-consistently within RISM and affected only by the choice of LJ interaction parameters (see below). The size of the electrode–electrolyte gap and the interfacial concentrations of electrolyte species also depend on the oxygen coverage at the Pt(111) slab. This effect is also taken into account self-consistently by the LJ interaction. With the outlined setup, we were able to reliably simulate the properties of the Pt(111)/electrolyte interface and to assess the performance of

ESM-RISM for this system.

In ESM-RISM, both the electrolyte–electrolyte and electrode–electrolyte interactions are described by classical interaction potentials (eq. (1)). For the electrolyte species, both LJ parameters and charges for the Coulomb interaction are those of the modified TIP5P water model or taken from the literature for the electrolyte ions (see Section II). The Coulomb interactions between the charges on the electrolyte species and on the electrode atoms depend on the charge density within the electrode computed by DFT [44]. In contrast, the LJ parameters of electrode atoms (Pt, O) have to be chosen manually. These parameters determine the electrode–electrolyte gap and the distribution of electrolyte at the interface via the correlation functions and closure relation. The choice of LJ interaction parameters for electrode atoms is not straightforward, since these are generally not transferable from one system to another. There is also only limited information on these parameters [83, 84]. We therefore tested different LJ parameterizations for the Pt atoms (see Table II) and compared electrolyte distribution functions at the Pt(111)/water interface to AIMD data [29, 85]. Fitting of LJ parameters to AIMD distribution functions is one way to improve the accuracy of ESM-RISM. Such an approach has been used recently to derive the LJ parameters for a Cu(100) electrode [48].

Figure 3 shows the interfacial water distribution functions computed with the different LJ parameter sets (see Table II) and with AIMD simulations [29, 85]. These are plane-averaged density profiles, where the absolute values refer to the area of our surface unit cell, which is 82.34 Å. ESM-RISM cannot reproduce the double peak structure (between 2 and 4 Å) obtained by AIMD [29, 85–88]. This is because the double peak reflects the structured surface water layer that cannot be reproduced by a microscopically averaging integral equation approach as implemented in RISM. Nevertheless, the overall shape of the distribution function is reproduced reasonably well, with the best match obtained with the LJ parameterization of Haruyama *et al.* [45], which had been used in the work of Fernandez-Alvarez and Eikerling [55], and was also used in all subsequently discussed calculations of this study. The width of the Pt(111)–water gap is very similar to the AIMD result (ca. 2 Å). The surface water layer in ESM-RISM exhibits one broad peak. Although it cannot quantitatively reproduce the bilayer AIMD feature (see discussion in the next section), its height and width are well consistent with the AIMD distribution, showing that the averaged near-surface water density and total width of the near-surface water layer are comparable.

TABLE II. Different applied Lennard-Jones parameters for the electrode Pt atoms.

| | $\varepsilon_{Pt}$ [kcal/mol] | $\sigma_{Pt}$ [Å] |
|---|---|---|
| Interface Force Field (IFF) [83, 84] | 7.80 | 2.53 |
| Universal Force Field (UFF) [89] | 0.08 | 2.45 |
| Pt–Xe interaction [45] | 1.66 | 2.65 |

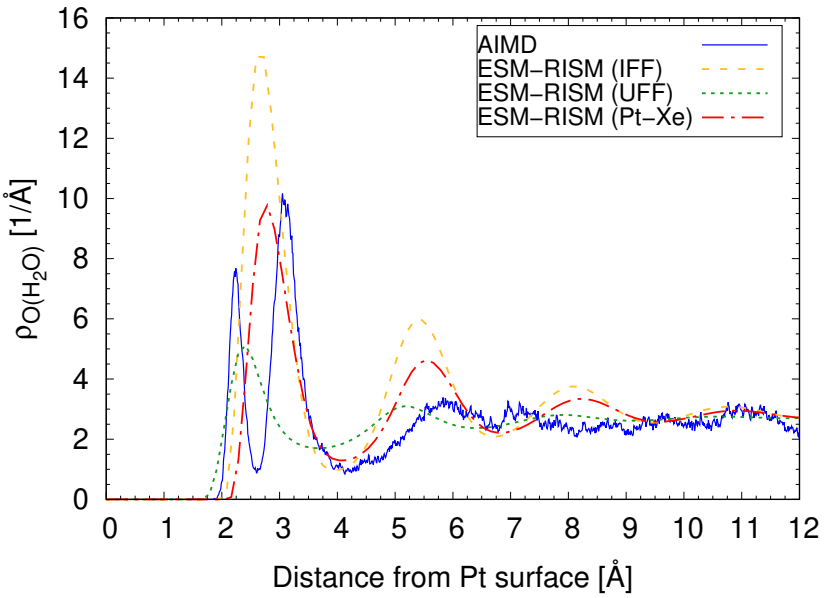


FIG. 3. Water density distribution functions at the Pt(111)/water interface computed with ESM-RISM using different LJ parameter sets for Pt (see Table II). The water density distribution is a function of the distance from the outermost layer of Pt atoms. The position of water molecules is represented by the position of water oxygen atoms. AIMD data were taken from refs. [29, 85]. ESM-RISM calculations were performed at 300 K solvent temperature.

Overall, as in the pure water case (see Figure 2), the accuracy of the results is limited by the statistical character of RISM: deviations from reference data are caused by local structuring of water that cannot be captured in this scheme. We also note that the simple LJ interaction potential is not optimal to describe the interatomic interactions quantitatively, and more sophisticated interatomic force-field schemes could further improve the performance of ESM-RISM.

### C. Quantum mechanically and classically treated parts of the system

#### 1. *Interface water structure*

As seen before in Figure 3, ESM-RISM (just like classical MD simulations, see Figure S7) cannot resolve the double peak in the water density distribution at the Pt(111)/water interface that was obtained with AIMD simulations [85–88]. This limits the applicability of ESM-RISM to surface reactions, where the arrangement of water molecules around adsorbed electroactive reactants plays a vital role. One solution for more accurate modeling of electrochemical reactions in these cases is to explicitly simulate the reactants with their hydration shell. The problems of implicit water models with the adequate description of solvent effects at interfaces have already been realized in previous studies [39, 90–93]. We thus tried to account for the local solvent effects within ESM-RISM by including the first interfacial water layer into the explicitly treated DFT region.

The explicit water layer was modeled by a static ice-like hexagonal water bilayer, a model which is commonly employed in DFT calculations of the wetted Pt(111) surface [46, 94, 95]. Such a structure with 2/3 ML water coverage has been observed experimentally at low temperature and in the case of a single surface water layer formed in ultrahigh vacuum [96]. These studies determined the water layer to be almost flat, representing more of a monolayer than a bilayer. Static DFT studies reproduce this small water layer thickness [97, 98]. In contrast, AIMD simulations, that were performed at room temperature [85–88], show the clear double peak (as depicted in Figure 3). We also notice that the areas of the two peaks composing the double peak are not identical, which is inconsistent with the perfect ice-like hexagonal water bilayer, where one half of the water molecules lie flatly on the surface and another half adsorb with H pointing towards the surface (H-down) or away from it (H-up). AIMD simulations show dynamic exchange between these two groups of water molecules [85] and between H-up and H-down configurations [88]. Sakong and Groß [29, 85] also observe rapid exchange of water molecules between the structured dynamic bilayer and the continuous, fluid-type water distribution (at distances larger than 4 Å).

Static DFT calculations cannot capture the dynamic nature of surface water layers. We thus considered the H-up and H-down configurations (see Figure 4) as limiting cases. Our focus was on the general effect of the explicit treatment of surface water molecules on interfacial

properties computed by ESM-RISM. Figure S8a shows that with static DFT/ESM-RISM calculations a structured first interfacial water layer is reproduced reasonably well, with the double peak feature, which, however, does not exactly match the AIMD result. Nevertheless, the implicit water distribution couples smoothly to the explicit part and the second solvent peak (around 6 Å from the Pt surface) matches the AIMD results well (better than in simulations without the explicit water layer). The Pt–O($H_2O$) distances in H-up and H-down configurations are slightly different, which is reflected by different positions of the double peaks using the two models. The true water orientation probably lies between these two limiting cases. These DFT/ESM-RISM calculations do not capture the exact separation between the two parts of the AIMD double peak. We notice, however, that reduced peak distances have been observed in other low temperature studies (far below 300 K), both experimental and computational [96–98], and may therefore be attributed to missing effects of thermal motion. DFT/ESM-RISM calculations thus yield an electrode–solvent gap that is slightly too large, which could affect computed interfacial properties. For comparison, we performed calculations with the $z$-coordinates of the oxygen atoms of the surface water bilayer fixed to the AIMD Pt-O($H_2O$) distances. Figure S8b shows that the so-obtained water distribution beyond the explicit layer (the part modeled by RISM) differs only slightly from that obtained using aforementioned setups.

### *2. Electrostatic potential at the interface*

Figure S9 illustrates the impact of the explicit water layer on the interfacial potential profile. Explicit treatment of near-surface water molecules leads to more pronounced peaks in electric potential. The potential at the outer Helmholtz plane (OHP) is also severely affected (see also Section III D). Fixing the positions of explicit water molecules to the AIMD positions results in a different potential profile (see Figure S9b), which reflects the distinct double peak in the surface water distribution (see Figure S8b). On the other hand, the potential profile beyond the explicit layer is hardly affected; it depends mainly on the position of the outer layer of the explicit double peak, which is very similar for both setups. The orientation of the hydrogen atoms (H-up vs. H-down) has a much larger effect on the potential profile beyond ∼3.5 Å from the Pt surface.

An explicit water layer is also important to reproduce the measured decrease of the work

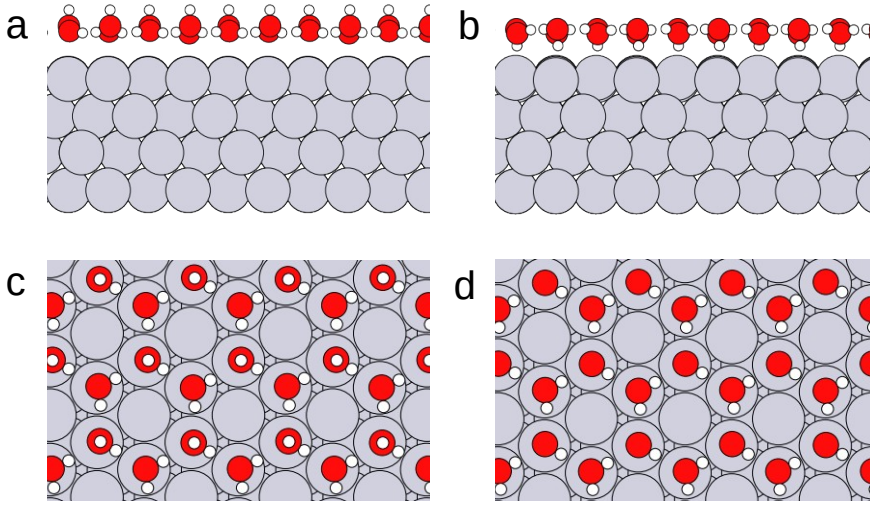


FIG. 4. Explicit surface water layer configurations, side and top views, for (a,c) H-up and (b,d) H-down configurations.

function of the wetted Pt(111) surface [99–101]. As shown in Table III, the implicit RISM solvent alone underestimates the change in the work function. This is due to the missing effects of surface water dipole orientation and polarization, i.e. interfacial charge transfer between surface water and Pt, which is captured only when the surface water molecules are computed explicitly [94, 101, 102]. Indeed, the best result is obtained with an explicit water layer in H-up configuration. The difference in the predicted work function shift with H-up and H-down explicit water layers arises from different dipole orientations in the two model cases, as found in other DFT studies [94, 101]. It dominates over the polarization effects for H-up and H-down configurations [101]. Nevertheless, AIMD simulations indicate that, when performing time averaging over different water configurations realized in the simulations, and thus averaging the dipole orientation, the polarization contribution is also an important factor [102].

The above discussion indicates that explicit treatment of the surface water layer is required to obtain a correct interfacial water structure with ESM-RISM. Describing the interaction between Pt and near-surface water molecules at the level of DFT is crucial in order to reproduce the realistic surface structure and interfacial electrostatic potential. The impact of the explicit water layer on other properties of the interface region will be discussed in the next section.

TABLE III. Work function change vs. vacuum for the Pt(111) surface in water solvent. [a]

| Setting | $\Delta\Phi$ [eV] |
|---|---|
| Implicit water | −0.23 |
| Implicit + 1 explicit layer (H-up) | −1.25 |
| Implicit + 1 explicit layer (H-down) | −0.26 |
| Experiment | −1.02 [99], −1.2 [100] |

[a] The work function is computed here as the difference between the Fermi level of the surface slab and the electrostatic potential in bulk solvent. This procedure deviates from the original definition of the work function, which defines it as the energy required to take an electron from the bulk of the metal to (electric-field free) vacuum.

### D. Potential at the outer Helmholtz plane

Experiments show that with an increase in applied electrode potential, an oxide layer forms at the Pt(111) surface [52]. It is thus important to take into account the oxygen coverage to correctly model electrochemical reactions at the Pt(111) surface. It impacts the electrolyte interfacial structure, solvent molecule orientation and local electrostatic potential. When computing the potential at the outer Helmholtz plane we therefore considered partially oxidized Pt(111) surfaces with oxygen coverages between 0 and 2/3 ML. The electrolyte consists of aqueous HCl with a concentration of 0.1 mol/L.

The theoretical description of electrocatalytic reactions requires knowledge of the electrostatic potential profile across the interface. The inner Helmholtz plane (IHP) is the first layer of adsorbed water and specifically adsorbed electrolyte ions, which is represented by the first peak in the solvent distribution functions in ESM-RISM (see e.g. Figure 3). The outer Helmholtz plane (OHP) is constituted by the first layer of non-specifically adsorbed (solvated) ions and the second water layer at the interface, and therefore is represented by the second peak in solvent distribution functions. The Helmholtz planes are important reaction planes for electrochemical reactions and the electrochemical conditions at their positions have to be known precisely. The potential at the OHP depends on near-surface solvent and electrolyte distribution and orientation, as well as on the oxygen coverage of Pt(111) and the metal surface charge. It is thus a suitable property to probe local reaction conditions at

the interface. Therefore, we evaluated the interfacial potential profile computed by ESM-RISM. We note that results of similar evaluations have been published before [54, 55] and here we compare our results with the outcome of those studies. Figure 5 shows the way the potential at the OHP is determined from the local interfacial potential profile. Our aim here is to assess the impact of ESM-RISM input variables and explicit treatment of surface water molecules on the value of the potential at the OHP.

Figure 6 shows the electrostatic potential at the outer Helmholtz plane as a function of oxygen coverage. We note that different adsorption geometries of adsorbed oxygen atoms result in slightly different values of potential at the OHP as computed with ESM-RISM ($\pm 0.05\,\mathrm{V}$). However, the trends as a function of potential are not affected. The potential at the OHP vs. oxygen coverage shows a non-monotonic behavior, as observed in previous DFT studies [55] and a mean-field approach by Huang *et al.* [53]. The differences from the previously published ESM-RISM results in ref. [55] stem from differences in the computational setup, namely from differences in the starting position of solvent, as we discussed in Section III B.

Figure 6 also illustrates the influence of an explicitly treated surface water layer on the outer Helmholtz potential. For the H-up configuration, the absolute potential at the OHP is much larger than in case of the H-down configuration and in the calculations with implicit electrolyte only. The explicit computation of the interfacial water structure seems to have a major impact on the electrolyte ion distribution near the interface and thus on the corresponding interfacial potential profile. As discussed before, the H-up and H-down structures can be considered as limiting cases of the real structure; the realistic outer Helmholtz potential is thus expected to lie between the H-up and H-down results. The overall agreement with the mean field model is not improved by the inclusion of the explicit water layer. This can be related to the fact that the explicit layer in our simulation setup does not contain charged species, which would significantly contribute to shaping the structure of the double layer. More sophisticated modeling is required to understand the differences between the results from the different approaches.

As shown in Figure 6, the different setups including calculations with the explicit water layer result in different values of the potential at the OHP. However, all predictions show a non-monotonic behavior, which is also seen in the measured metal charging relation [103]. This shows that the potential-dependent oxygen coverage at Pt(111) causes the peculiar

non-monotonic effects on the interfacial potential. Note that the potential at the OHP as considered here is averaged over the plane perpendicular to the Pt surface. Variations in this plane are of course possible, but not resolved here. This is one aspect that hinders a more detailed comparison between the results from different simulation setups and models. To include the effects of an applied potential – beyond the resulting oxygen coverage – we applied the ESM-RISM potentiostat to perform grand canonical calculations, as described in the next section.

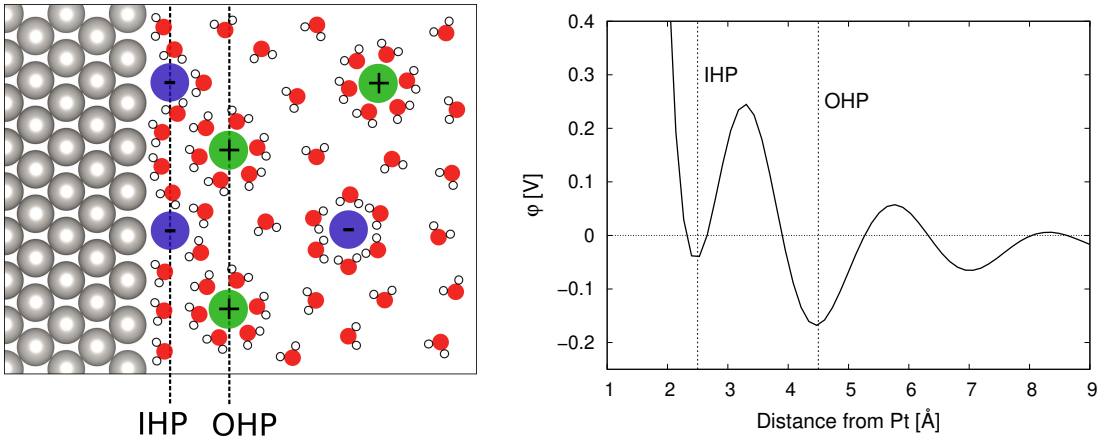


(a) (b)

FIG. 5. (a) Schematic representation of inner (IHP) and outer (OHP) Helmholtz planes at the Pt(111)/electrolyte interface. (b) Plane-averaged local potential at the bare Pt(111)/electrolyte interface, computed with ESM-RISM.

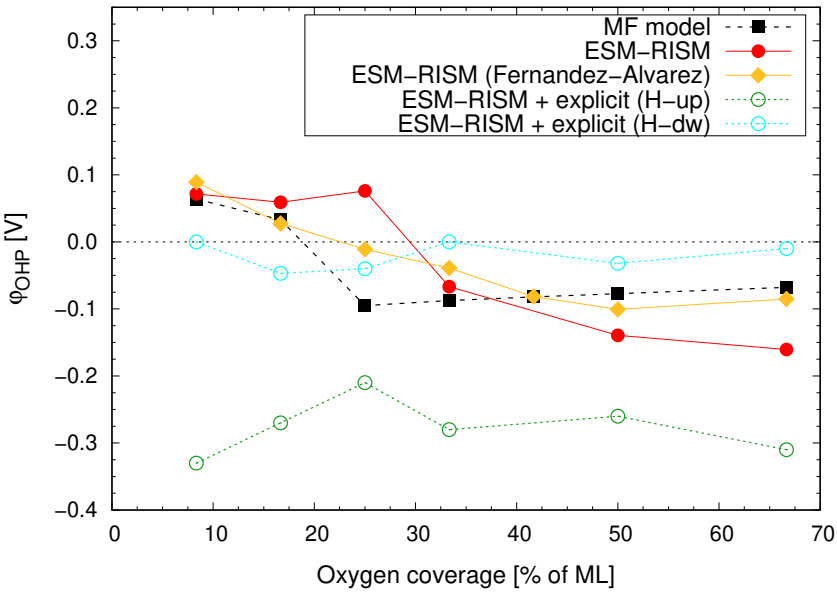


FIG. 6. Potential at the outer Helmholtz plane for the oxidized Pt(111)/electrolyte interface (c(HCl) = 0.1 mol/L). Mean field (MF) model by Huang *et al.* [54]. ESM-RISM results (implicit electrolyte only) with smaller DFT cell length and `laue_starting_right` parameter obtained from energy minimization by Fernandez-Alvarez and Eikerling [55]. Curves obtained with one explicitly treated water layer in H-up and H-down configurations are shown as well.

### E. Grand canonical ESM-RISM simulations and metal charging relation

The ESM-RISM implementation includes a potentiostat scheme that allows to apply a potential in the grand canonical ensemble and thus compute realistic electrochemical interfaces at a given electrode potential [26]. In this framework, the resulting charge of the metal slab is compensated by the electrolyte charge of equal size and opposite sign.

For the case of the partially oxidized Pt(111)/electrolyte interface, the oxygen coverage can be pinned to the metal potential by using the experimental surface coverage-vs-potential data [54, 55]. Following the mean field model [54], we assume that the uncharged bare Pt(111) surface corresponds to the potential of zero charge (pzc), which is 0.3 V vs. SHE. The functional relationship between oxygen coverage and potential is summarized in Table IV. Only when taking into account both the applied potential and the corresponding oxygen coverage, the realistic conditions at the Pt(111)/electrolyte interface can be reproduced. The calculations with applied potential were performed here assuming implicit aqueous HCl

electrolytes with concentrations of 0.1 and 1 mol/L.

Charge analysis of the oxidized Pt(111) surface slabs showed that charges are entirely located at surface Pt atoms and adsorbed O atoms. This corresponds to the expected and realistic charge distribution.

Figure 7 shows the computed surface ion density profiles for the different applied potentials for $Cl^-$ and $H_3O^+$ ions in the electrolyte. The different peaks represent the alternating charged layers of electrolyte ions at the interface. The obtained trends clearly reflect the electrostatic effects of the positive slab charge (representing the positively charged Pt electrode). For example, a depletion of $H_3O^+$ ions in the interface region with increasing positive electrode charge is clearly visible.

The electrode charges per area of the oxidized Pt(111) surface at different potentials are shown in Figure 8. The metal charge as a function of the electrode potential exhibits a non-monotonic trend, which was also observed in seminal experiments by Frumkin and Petrii [103]. As expected, the higher electrolyte concentration leads to slightly higher metal charges. Vital features of the metal charging relation, i.e. $\sigma$ plotted as a function of $\varphi_\mathrm{M}$, are in agreement with the prediction by the mean-field (MF) model of Huang *et al.* [53] (black dashed line in Figure 8) and experimental data [103]. As the electrode potential increases from the potential of zero charge (pzc), the surface charge density increases monotonically, reaching a maximum at 0.8 V vs. SHE (at 0.55 V vs. SHE in the MF model). Upon further increase of $\varphi_\mathrm{M}$, $\sigma$ decreases to a minimum at 1.0 V vs. SHE (0.8 V vs. SHE in the MF model). We notice that the second pzc, as measured [103] and reproduced by the MF model [53], is not seen with ESM-RISM.

For comparison, Figure S12 depicts the metal charging relation for the non-oxidized Pt(111)/electrolyte interface. For the bare electrode surface, a linear metal charging relation is obtained, which reflects charge accumulated in the double layer and is well consistent with the double layer charge contribution to the total charge, as modeled by Huang *et al.* [53]. We note, however, that bare Pt(111) surfaces do not exist in the respective potential range.

Huang *et al.* [53] attributed the non-monotonic charging behaviour, with a second pzc at about 0.75 V vs. SHE, to the impact of surface oxide dipoles. Our results from ESM-RISM support this interpretation, since without the surface oxide layer the peculiar non-monotonic shape of the metal charging relation is not reproduced (see Figure S12). Further, in the MF model, the increase in charge for potentials higher than 0.8 V vs. SHE is explained by

saturation of oxide species at the Pt surface [53]. The quantitative disagreement in metal charging relations between ESM-RISM and the MF model indicates that potential effects are screened differently in the two approaches. Differences in potential screening by the oxide layer, but also by the layer of interfacial water dipoles or the diffuse ionic layer are possible and should be evaluated in more detail in follow-up studies. In this regard, the grey dashed line in Figure 8 illustrates the sensitivity of the interfacial potential distribution and surface charging to parameterization of the MF model [104]. With a smaller fractional charge number of the oxide dipole, as used in the modified parameterization [104], the quantitative agreement with the ESM-RISM results is improved.

Both, ESM-RISM and MF model rely on assumptions and approximations about structural organization and polarization effects in the interface region. These assumptions will have to be scrutinized and fine-tuned in future work. However, the qualitative agreement between the approaches that has been achieved to date is encouraging. The crucial role of surface oxide formation in determining interface properties and local reaction conditions is clearly evident.

At small electrode potential (below ca. 0.6 V vs. SHE, where the oxygen coverage is zero), the double layer capacitance for the Pt(111)/electrolyte interface can be estimated from the slope of the metal charge per area vs. applied potential. This simple estimate yields interfacial capacitances of 24 and 33 $\mu$F/cm$^2$ for electrolyte concentrations of 0.1 and 1 mol/L, respectively. These values are in agreement with the experimental value of 20 $\mu$F/cm$^2$ [105] and results of other computational studies [106]. ESM-RISM reproduces the linear capacitive response of metals that are not covered with adsorbates.

TABLE IV. Oxygen coverage as a function of the applied potential as computed by the mean field model by Huang *et al.* [54]. The pzc is 0.3 V vs. SHE. 1 monolayer (ML) of oxygen coverage corresponds to 12 adsorbed atoms per unit cell.

| # ads. O atoms | coverage [% of ML] | $\varphi_{\mathrm{M}}$ vs. SHE [V] |
|---|---|---|
| 0 | 0 | 0.30 |
| 0 | 0 | 0.45 |
| 0 | 0 | 0.55 |
| 1 | 8.3 | 0.65 |
| 2 | 16.7 | 0.73 |
| 3 | 25.0 | 0.85 |
| 4 | 33.3 | 0.90 |
| 6 | 50.0 | 0.96 |
| 8 | 66.7 | 1.00 |
| 9 | 75.0 | 1.10 |

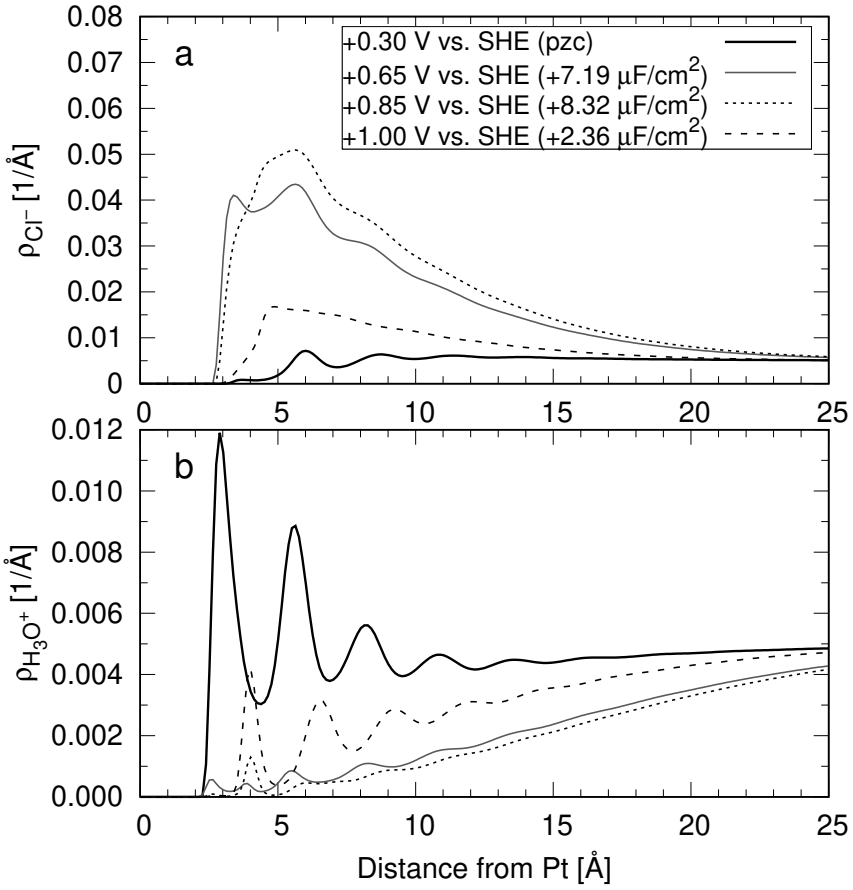


FIG. 7. Density profiles for (a) $Cl^-$ and (b) $H_3O^+$ electrolyte ions (c(HCl) = 0.1 mol/L) computed with ESM-RISM at different electrode potentials. Surface charges per area are given in brackets. The Pt(111) surface is partially oxidized according to the applied potential; for coverages see Table IV. Data for all computed potentials are available in Figures S9 and S10.

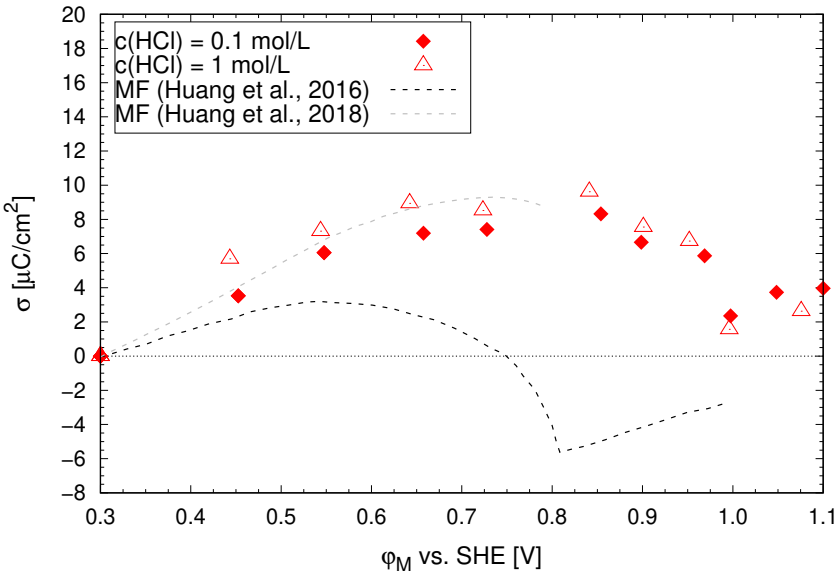


FIG. 8. Surface charge vs. electrode potential for the oxidized Pt(111)/electrolyte interface with different electrolyte concentrations. The oxygen coverages for the different potentials are those from Table IV. Slight deviations arise from the charge optimization procedure. For potentials higher than 1.0 vs. SHE, we performed calculations with oxygen coverages of both 66.7 % and 75.0 %, because oxygen coverages larger than 66.7 % tend to favor Pt dissolution [107, 108]. The impact on the results was insignificant. Data for the mean-field model (MF) by Huang *et al.* [53] at pH 1.2 (black dashed line) and with a smaller fractional charge number of the oxide dipole, at pH 1 [104] (light grey dashed line).

## IV. SUMMARY AND CONCLUSIONS

We presented an in-depth evaluation of the abilities of ESM-RISM to reproduce properties of electrochemical interfaces. As a demonstration case we studied the interface between a partially oxidized Pt(111) surface and an aqueous HCl electrolyte solution. In contrast to standard cavity-based continuum solvation models, ESM-RISM provides more realistic electrolyte distribution functions at the interface. Grand canonical simulations with the potentiostat enabled us to model the interface under applied potential.

We have shown that interface properties are highly sensitive to the choice of ESM-RISM parameters. First of all, the results depend on the parameterization of the electrode–electrolyte interactions, described with Lennard-Jones potentials in ESM-RISM, which self-

consistently determine the electrode–electrolyte gap. The LJ interaction parameters were selected to reproduce the AIMD interfacial solvent density profiles. We also demonstrated that the structured interfacial water layer has to be explicitly computed at the level of DFT in order to capture the interfacial electrolyte structure and resulting electrostatic potential profiles. The implicit electrolyte, as modeled by RISM, smoothly couples to the explicit water layer and such a hybrid approach consistently describes the electrolyte structure.

Regarding the electrochemical parameters, the ESM-RISM framework reproduces the effect of a surface oxide layer on the outer Helmholtz potential. Only by accounting for the oxide layer, we were able to reproduce the non-monotonic metal charging relation that is known from experiments for the partially oxidized Pt(111)/electrolyte interface. The thorough testing of ESM-RISM for the Pt(111)/electrolyte interface indicates that when correctly set up, this method can result in a quantitative level prediction of properties of electrochemical interfaces, including the structure of the double layer, the interfacial potential variation and the metal charging relation.

## ACKNOWLEDGMENTS

Computational resources provided by the Jülich Aachen Research Alliance-Center for Simulation and Data Science (JARA-CSD, projects jara0037 and JIEK61) are gratefully acknowledged. We thank Minoru Otani, Victor Fernandez-Alvarez and Jun Huang for helpful discussions on electrochemical interface modeling. We also thank Sung Sakong for sharing the AIMD raw data and Oskar Cheong for running the classical MD simulation.

---

[1] A. Gallo, J. Simões-Moreira, H. Costa, M. Santos, and E. Moutinho dos Santos, Energy storage in the energy transition context: A technology review, Renewable and Sustainable Energy Reviews **65**, 800 (2016).

[2] N. Kittner, F. Lill, and D. M. Kammen, Energy storage deployment and innovation for the clean energy transition, Nature Energy **2**, 10.1038/nenergy.2017.125 (2017).

[3] A. Kalair, N. Abas, M. S. Saleem, A. R. Kalair, and N. Khan, Role of energy storage systems in energy transition from fossil fuels to renewables, Energy Storage **3**, e135 (2021).

[4] N. S. Lewis and D. G. Nocera, Powering the planet: Chemical challenges in solar energy utilization, Proceedings of the National Academy of Sciences **103**, 15729 (2006).

[5] N. Armaroli and V. Balzani, Solar electricity and solar fuels: Status and perspectives in the context of the energy transition, Chemistry – A European Journal **22**, 32 (2016).

[6] O. M. Magnussen and A. Groß, Toward an atomic-scale understanding of electrochemical interface structure and dynamics, Journal of the American Chemical Society **141**, 4777 (2019), pMID: 30768905.

[7] A. Groß, Grand-canonical approaches to understand structures and processes at electrochemical interfaces from an atomistic perspective, Current Opinion in Electrochemistry **27**, 100684 (2021).

[8] H. Helmholtz, Studien über electrische grenzschichten, Annalen der Physik **243**, 337 (1879).

[9] M. Gouy, Sur la constitution de la charge électrique à la surface d'un électrolyte, Journal de Physique Théorique et Appliquée **9**, 457 (1910).

[10] D. L. Chapman, Li. a contribution to the theory of electrocapillarity, The London, Edinburgh, and Dublin Philosophical Magazine and Journal of Science **25**, 475 (1913).

[11] O. Stern, Zur theorie der elektrolytischen doppelschicht, Zeitschrift für Elektrochemie und angewandte physikalische Chemie **30**, 508 (1924).

[12] D. C. Grahame, The electrical double layer and the theory of electrocapillarity., Chemical Reviews **41**, 441 (1947), pMID: 18895519.

[13] M. J. Eslamibidgoli, J. Huang, T. Kadyk, A. Malek, and M. Eikerling, How theory and simulation can drive fuel cell electrocatalysis, Nano Energy **29**, 334 (2016), electrocatalysis.

[14] S. Jahn and P. M. Kowalski, Theoretical approaches to structure and spectroscopy of earth materials, Rev. Mineral. Geochem. **78**, 691 (2014).

[15] K. Schwarz and R. Sundararaman, The electrochemical interface in first-principles calculations, Surface Science Reports **75**, 100492 (2020).

[16] M. J. Eslamibidgoli and M. H. Eikerling, Approaching the self-consistency challenge of electrocatalysis with theory and computation, Current Opinion in Electrochemistry **9**, 189 (2018).

[17] J. K. Nørskov, J. Rossmeisl, A. Logadottir, L. Lindqvist, J. R. Kitchin, T. Bligaard, and H. Jónsson, Origin of the overpotential for oxygen reduction at a fuel-cell cathode, The Journal of Physical Chemistry B **108**, 17886 (2004).

[18] J.-S. Filhol and M. Neurock, Elucidation of the electrochemical activation of water over pd by first principles, Angewandte Chemie International Edition **45**, 402 (2006).

[19] C. D. Taylor, S. A. Wasileski, J.-S. Filhol, and M. Neurock, First principles reaction modeling of the electrochemical interface: Consideration and calculation of a tunable surface potential from atomic and electronic structure, Phys. Rev. B **73**, 165402 (2006).

[20] M. Otani and O. Sugino, First-principles calculations of charged surfaces and interfaces: A plane-wave nonrepeated slab approach, Phys. Rev. B **73**, 115407 (2006).

[21] E. Skúlason, G. S. Karlberg, J. Rossmeisl, T. Bligaard, J. Greeley, H. Jónsson, and J. K. Nørskov, Density functional theory calculations for the hydrogen evolution reaction in an electrochemical double layer on the pt(111) electrode, Phys. Chem. Chem. Phys. **9**, 3241 (2007).

[22] G. Kastlunger, P. Lindgren, and A. A. Peterson, Controlled-potential simulation of elementary electrochemical reactions: Proton discharge on metal surfaces, The Journal of Physical Chemistry C **122**, 12771 (2018).

[23] K. Chan and J. K. Nørskov, Electrochemical barriers made simple, The Journal of Physical Chemistry Letters **6**, 2663 (2015).

[24] M. Nielsen, M. E. Björketun, M. H. Hansen, and J. Rossmeisl, Towards first principles modeling of electrochemical electrode–electrolyte interfaces, Surface Science **631**, 2 (2015), surface Science and Electrochemistry - 20 years later.

[25] J. A. Gauthier, C. F. Dickens, S. Ringe, and K. Chan, Practical considerations for continuum models applied to surface electrochemistry, ChemPhysChem **20**, 3074 (2019).

[26] N. Bonnet, T. Morishita, O. Sugino, and M. Otani, First-principles molecular dynamics at a constant electrode potential, Phys. Rev. Lett. **109**, 266101 (2012).

[27] A. Y. Lozovoi, A. Alavi, J. Kohanoff, and R. M. Lynden-Bell, Ab initio simulation of charged slabs at constant chemical potential, The Journal of Chemical Physics **115**, 1661 (2001).

[28] N. G. Hörmann, O. Andreussi, and N. Marzari, Grand canonical simulations of electrochemical interfaces in implicit solvation models, The Journal of Chemical Physics **150**, 041730 (2019).

[29] S. Sakong and A. Groß, The electric double layer at metal-water interfaces revisited based on a charge polarization scheme, The Journal of Chemical Physics **149**, 084705 (2018).

[30] J.-B. Le and J. Cheng, Modeling electrochemical interfaces from ab initio molecular dy-

namics: water adsorption on metal surfaces at potential of zero charge, Current Opinion in Electrochemistry **19**, 129 (2020), fundamental and Theoretical Electrochemistry, Bioelectrochemistry.

[31] L.-P. Wang and T. Van Voorhis, A polarizable qm/mm explicit solvent model for computational electrochemistry in water, Journal of Chemical Theory and Computation **8**, 610 (2012), pMID: 26596609.

[32] S. Dohm, E. Spohr, and M. Korth, Developing adaptive qm/mm computer simulations for electrochemistry, Journal of Computational Chemistry **38**, 51 (2017).

[33] J. Tomasi and M. Persico, Molecular interactions in solution: an overview of methods based on continuous distributions of the solvent, Chemical Reviews **94**, 2027 (1994).

[34] O. Andreussi, I. Dabo, and N. Marzari, Revised self-consistent continuum solvation in electronic-structure calculations, The Journal of Chemical Physics **136**, 064102 (2012).

[35] K. Mathew, R. Sundararaman, K. Letchworth-Weaver, T. A. Arias, and R. G. Hennig, Implicit solvation model for density-functional study of nanocrystal surfaces and reaction pathways, The Journal of Chemical Physics **140**, 084106 (2014).

[36] R. Sundararaman, K. A. Schwarz, K. Letchworth-Weaver, and T. A. Arias, Spicing up continuum solvation models with salsa: The spherically averaged liquid susceptibility ansatz, The Journal of Chemical Physics **142**, 054102 (2015).

[37] R. Sundararaman and W. A. Goddard, The charge-asymmetric nonlocally determined local-electric (candle) solvation model, The Journal of Chemical Physics **142**, 064107 (2015).

[38] I. Borukhov, D. Andelman, and H. Orland, Steric effects in electrolytes: A modified poisson-boltzmann equation, Phys. Rev. Lett. **79**, 435 (1997).

[39] R. Sundararaman and K. Schwarz, Evaluating continuum solvation models for the electrode-electrolyte interface: Challenges and strategies for improvement, The Journal of Chemical Physics **146**, 084111 (2017).

[40] O. Andreussi, N. G. Hörmann, F. Nattino, G. Fisicaro, S. Goedecker, and N. Marzari, Solvent-aware interfaces in continuum solvation, Journal of Chemical Theory and Computation **15**, 1996 (2019).

[41] D. Chandler and H. C. Andersen, Optimized cluster expansions for classical fluids. ii. theory of molecular liquids, The Journal of Chemical Physics **57**, 1930 (1972).

[42] J. P. Hansen and I. R. McDonald, *Theory of Simple Liquids* (Academic, London, 1976).

[43] S. A. Petrosyan, J.-F. Briere, D. Roundy, and T. A. Arias, Joint density-functional theory for electronic structure of solvated systems, Phys. Rev. B **75**, 205105 (2007).

[44] S. Nishihara and M. Otani, Hybrid solvation models for bulk, interface, and membrane: Reference interaction site methods coupled with density functional theory, Phys. Rev. B **96**, 115429 (2017), and Supplementary Information.

[45] J. Haruyama, T. Ikeshoji, and M. Otani, Electrode potential from density functional theory calculations combined with implicit solvation theory, Phys. Rev. Materials **2**, 095801 (2018).

[46] S. Sakong, M. Naderian, K. Mathew, R. G. Hennig, and A. Groß, Density functional theory study of the electrochemical interface between a pt electrode and an aqueous electrolyte using an implicit solvent method, The Journal of Chemical Physics **142**, 234107 (2015).

[47] J. Haruyama, T. Ikeshoji, and M. Otani, Analysis of lithium insertion/desorption reaction at interfaces between graphite electrodes and electrolyte solution using density functional + implicit solvation theory, The Journal of Physical Chemistry C **122**, 9804 (2018).

[48] S. E. Weitzner, S. A. Akhade, J. B. Varley, B. C. Wood, M. Otani, S. E. Baker, and E. B. Duoss, Toward engineering of solution microenvironments for the co2 reduction reaction: Unraveling ph and voltage effects from a combined density-functional–continuum theory, The Journal of Physical Chemistry Letters **11**, 4113 (2020), pMID: 32343146.

[49] K. Kano, S. Hagiwara, T. Igarashi, and M. Otani, Study on the free corrosion potential at an interface between an al electrode and an acidic aqueous nacl solution through density functional theory combined with the reference interaction site model, Electrochimica Acta **377**, 138121 (2021).

[50] V. Stamenkovic, B. S. Mun, K. J. Mayrhofer, P. N. Ross, N. M. Markovic, J. Rossmeisl, J. Greeley, and J. K. Nørskov, Changing the activity of electrocatalysts for oxygen reduction by tuning the surface electronic structure, Angewandte Chemie **118**, 2963 (2006).

[51] Z. A. C. Ramli and S. K. Kamarudin, Platinum-based catalysts on various carbon supports and conducting polymers for direct methanol fuel cell applications: a review, Nanoscale Research Letters **13**, 10.1186/s11671-018-2799-4 (2018).

[52] A. Berná, V. Climent, and J. M. Feliu, New understanding of the nature of oh adsorption on pt(111) electrodes, Electrochemistry Communications **9**, 2789 (2007).

[53] J. Huang, A. Malek, J. Zhang, and M. H. Eikerling, Non-monotonic surface charging behavior of platinum: A paradigm change, The Journal of Physical Chemistry C **120**, 13587 (2016).

[54] J. Huang, J. Zhang, and M. Eikerling, Unifying theoretical framework for deciphering the oxygen reduction reaction on platinum, Phys. Chem. Chem. Phys. **20**, 11776 (2018).

[55] V. M. Fernandez-Alvarez and M. H. Eikerling, Interface properties of the partially oxidized pt(111) surface using hybrid dft–solvation models, ACS Applied Materials & Interfaces **11**, 43774 (2019), pMID: 31650835.

[56] P. Giannozzi, S. Baroni, N. Bonini, M. Calandra, R. Car, C. Cavazzoni, D. Ceresoli, G. L. Chiarotti, M. Cococcioni, I. Dabo, A. D. Corso, S. de Gironcoli, S. Fabris, G. Fratesi, R. Gebauer, U. Gerstmann, C. Gougoussis, A. Kokalj, M. Lazzeri, L. Martin-Samos, N. Marzari, F. Mauri, R. Mazzarello, S. Paolini, A. Pasquarello, L. Paulatto, C. Sbraccia, S. Scandolo, G. Sclauzero, A. P. Seitsonen, A. Smogunov, P. Umari, and R. M. Wentzcovitch, QUANTUM ESPRESSO: a modular and open-source software project for quantum simulations of materials, Journal of Physics: Condensed Matter **21**, 395502 (2009).

[57] J. P. Perdew, M. Ernzerhof, and K. Burke, Rationale for mixing exact exchange with density functional approximations, The Journal of Chemical Physics **105**, 9982 (1996).

[58] Y. Zhang and W. Yang, Comment on "generalized gradient approximation made simple", Phys. Rev. Lett. **80**, 890 (1998).

[59] S. Grimme, J. Antony, S. Ehrlich, and H. Krieg, A consistent and accurate ab initio parametrization of density functional dispersion correction (dft-d) for the 94 elements h-pu, The Journal of Chemical Physics **132**, 154104 (2010).

[60] B. Hammer, L. B. Hansen, and J. K. Nørskov, Improved adsorption energetics within density-functional theory using revised perdew-burke-ernzerhof functionals, Phys. Rev. B **59**, 7413 (1999).

[61] K. Yang, J. Zheng, Y. Zhao, and D. G. Truhlar, Tests of the rpbe, revpbe, $\tau$-hcthhyb, $\omega$b97x-d, and mohlyp density functional approximations and 29 others against representative databases for diverse bond energies and barrier heights in catalysis, The Journal of Chemical Physics **132**, 164117 (2010).

[62] K. Tonigold and A. Groß, Dispersive interactions in water bilayers at metallic surfaces: A comparison of the pbe and rpbe functional including semiempirical dispersion corrections, Journal of Computational Chemistry **33**, 695 (2012).

[63] H. A. Lorentz, Ueber die anwendung des satzes vom virial in der kinetischen theorie der gase, Annalen der Physik **248**, 127 (1881).

[64] A. Kovalenko and F. Hirata, Three-dimensional density profiles of water in contact with a solute of arbitrary shape: a rism approach, Chemical Physics Letters **290**, 237 (1998).

[65] A. Kovalenko and F. Hirata, Self-consistent description of a metal–water interface by the kohn–sham density functional theory and the three-dimensional reference interaction site model, The Journal of Chemical Physics **110**, 10095 (1999).

[66] M. W. Mahoney and W. L. Jorgensen, A five-site model for liquid water and the reproduction of the density anomaly by rigid, nonpolarizable potential functions, The Journal of Chemical Physics **112**, 8910 (2000).

[67] W. F. v. G. H. J. C. Berendsen, J. P. M. Postma and J. Hermans, *Intermolecular Forces*, edited by B. Pullman (Reidel, Dordrecht, 1981) p. 331.

[68] M. Matsugami, N. Yoshida, and F. Hirata, Theoretical characterization of the "ridge" in the supercritical region in the fluid phase diagram of water, The Journal of Chemical Physics **140**, 104511 (2014).

[69] A. Kovalenko and F. Hirata, First-principles realization of a van der waals–maxwell theory for water, Chemical Physics Letters **349**, 496 (2001).

[70] F. Hirata and R. M. Levy, Ionic association in methanol and related solvents: an extended rism analysis, The Journal of Physical Chemistry **91**, 4788 (1987).

[71] R. T. Cygan, J.-J. Liang, and A. G. Kalinichev, Molecular models of hydroxide, oxyhydroxide, and clay phases and the development of a general force field, The Journal of Physical Chemistry B **108**, 1255 (2004).

[72] H. J. Monkhorst and J. D. Pack, Special points for Brillouin-zone integrations, Phys. Rev. B **13**, 5188 (1976).

[73] D. E. Smith and L. X. Dang, Computer simulations of nacl association in polarizable water, The Journal of Chemical Physics **100**, 3757 (1994).

[74] G. Chuev, S. Chiodo, S. Erofeeva, M. Fedorov, N. Russo, and E. Sicilia, A quasilinear rism approach for the computation of solvation free energy of ionic species, Chemical Physics Letters **418**, 485 (2006).

[75] W. L. Jorgensen, J. Chandrasekhar, J. D. Madura, R. W. Impey, and M. L. Klein, Comparison of simple potential functions for simulating liquid water, The Journal of Chemical Physics **79**, 926 (1983).

[76] M. Sprik, J. Hutter, and M. Parrinello, Ab initio molecular dynamics simulation of liquid

water: Comparison of three gradient-corrected density functionals, The Journal of Chemical Physics **105**, 1142 (1996).

[77] A. D. Boese, Density functional theory and hydrogen bonds: Are we there yet?, ChemPhysChem **16**, 978 (2015).

[78] A. K. Soper, The radial distribution functions of water as derived from radiation total scattering experiments: Is there anything we can say for sure?, ISRN Physical Chemistry **2013**, 1 (2013).

[79] S. Zhao, Y. Liu, H. Liu, and J. Wu, Site-site direct correlation functions for three popular molecular models of liquid water, The Journal of Chemical Physics **139**, 064509 (2013).

[80] A. Ben-Naim and Y. Marcus, Solvation thermodynamics of nonionic solutes, The Journal of Chemical Physics **81**, 2016 (1984).

[81] V. Feldman, A. Kornyshev, and M. Partenskiĭ, Density functional simulation of interfacial relaxation and capacity of a model metal/electrolyte interface, Solid State Communications **53**, 157 (1985).

[82] J. Huang, P. Li, and S. Chen, Potential of zero charge and surface charging relation of metal-solution interphases from a constant-potential jellium-poisson-boltzmann model, Phys. Rev. B **101**, 125422 (2020).

[83] H. Heinz, T.-J. Lin, R. Kishore Mishra, and F. S. Emami, Thermodynamically consistent force fields for the assembly of inorganic, organic, and biological nanostructures: The interface force field, Langmuir **29**, 1754 (2013).

[84] H. Heinz, R. A. Vaia, B. L. Farmer, and R. R. Naik, Accurate simulation of surfaces and interfaces of face-centered cubic metals using 12-6 and 9-6 lennard-jones potentials, The Journal of Physical Chemistry C **112**, 17281 (2008).

[85] S. Sakong and A. Groß, Water structures on a Pt(111) electrode from ab initio molecular dynamic simulations for a variety of electrochemical conditions, Physical Chemistry Chemical Physics **22**, 10431 (2020).

[86] H. H. Kristoffersen, T. Vegge, and H. A. Hansen, Oh formation and h2 adsorption at the liquid water–pt(111) interface, Chem. Sci. **9**, 6912 (2018).

[87] P. Li, J. Huang, Y. Hu, and S. Chen, Establishment of the potential of zero charge of metals in aqueous solutions: Different faces of water revealed by ab initio molecular dynamics simulations, The Journal of Physical Chemistry C **125**, 3972 (2021).

[88] S. Schnur and A. Groß, Properties of metal–water interfaces studied from first principles, New Journal of Physics **11**, 125003 (2009).

[89] A. K. Rappe, C. J. Casewit, K. S. Colwell, W. A. Goddard, and W. M. Skiff, Uff, a full periodic table force field for molecular mechanics and molecular dynamics simulations, Journal of the American Chemical Society **114**, 10024 (1992).

[90] H. H. Heenen, J. A. Gauthier, H. H. Kristoffersen, T. Ludwig, and K. Chan, Solvation at metal/water interfaces: An ab initio molecular dynamics benchmark of common computational approaches, The Journal of Chemical Physics **152**, 144703 (2020).

[91] A. M. Maldonado, S. Hagiwara, T. H. Choi, F. Eckert, K. Schwarz, R. Sundararaman, M. Otani, and J. A. Keith, Quantifying uncertainties in solvation procedures for modeling aqueous phase reaction mechanisms, The Journal of Physical Chemistry A **125**, 154 (2021), pMID: 33393781.

[92] S. Lange, P. M. Kowalski, M. Pšeničkа, M. Klinkenberg, S. Rohmen, D. Bosbach, and G. Deissmann, Uptake of 226ra in cementitious systems: A complementary solution chemistry and atomistic simulation study, Applied Geochemistry **96**, 204 (2018).

[93] N. G. Hörmann, Z. Guo, F. Ambrosio, O. Andreussi, A. Pasquarello, and N. Marzari, Absolute band alignment at semiconductor-water interfaces using explicit and implicit descriptions for liquid water, npj Computational Materials **5**, 10.1038/s41524-019-0238-4 (2019).

[94] A. Malek and M. H. Eikerling, Chemisorbed oxygen at pt(111): a DFT study of structural and electronic surface properties, Electrocatalysis **9**, 370 (2017).

[95] M. J. Eslamibidgoli and M. H. Eikerling, Electrochemical formation of reactive oxygen species at pt (111)—a density functional theory study, ACS Catalysis **5**, 6090 (2015).

[96] H. Ogasawara, B. Brena, D. Nordlund, M. Nyberg, A. Pelmenschikov, L. G. M. Pettersson, and A. Nilsson, Structure and bonding of water on pt(111), Phys. Rev. Lett. **89**, 276102 (2002).

[97] S. Meng, E. G. Wang, and S. Gao, Water adsorption on metal surfaces: A general picture from density functional theory studies, Phys. Rev. B **69**, 195404 (2004).

[98] T. Jacob and W. A. Goddard, Agostic interactions and dissociation in the first layer of water on pt(111), Journal of the American Chemical Society **126**, 9360 (2004), pMID: 15281827.

[99] J. Heras and L. Viscido, Work function changes upon water contamination of metal surfaces, Applications of Surface Science **4**, 238 (1980).

[100] E. Langenbach, A. Spitzer, and H. Lüth, The adsorption of water on pt(111) studied by irreflection and uv-photoemission spectroscopy, Surface Science **147**, 179 (1984).

[101] V. Tripkovic, M. E. Björketun, E. Skúlason, and J. Rossmeisl, Standard hydrogen electrode and potential of zero charge in density functional calculations, Phys. Rev. B **84**, 115452 (2011).

[102] J. Le, M. Iannuzzi, A. Cuesta, and J. Cheng, Determining potentials of zero charge of metal electrodes versus the standard hydrogen electrode from density-functional-theory-based molecular dynamics, Phys. Rev. Lett. **119**, 016801 (2017).

[103] A. Frumkin and O. Petrii, Potentials of zero total and zero free charge of platinum group metals, Electrochimica Acta **20**, 347 (1975).

[104] J. Huang, T. Zhou, J. Zhang, and M. Eikerling, Double layer of platinum electrodes: Non-monotonic surface charging phenomena and negative double layer capacitance, The Journal of Chemical Physics **148**, 044704 (2018).

[105] T. Pajkossy and D. Kolb, Double layer capacitance of pt(111) single crystal electrodes, Electrochimica Acta **46**, 3063 (2001).

[106] K. Letchworth-Weaver and T. A. Arias, Joint density functional theory of the electrode-electrolyte interface: Application to fixed electrode potentials, interfacial capacitances, and potentials of zero charge, Phys. Rev. B **86**, 075140 (2012).

[107] A. A. Topalov, S. Cherevko, A. R. Zeradjanin, J. C. Meier, I. Katsounaros, and K. J. J. Mayrhofer, Towards a comprehensive understanding of platinum dissolution in acidic media, Chem. Sci. **5**, 631 (2014).

[108] M. J. Eslamibidgoli and M. H. Eikerling, Atomistic mechanism of pt extraction at oxidized surfaces: Insights from DFT, Electrocatalysis **7**, 345 (2016).